

Local voltage mapping of solar cells in the presence of localized radiative defects

Cite as: Appl. Phys. Lett. 121, 031102 (2022); doi: 10.1063/5.0097572

Submitted: 29 April 2022 · Accepted: 2 July 2022 ·

Published Online: 18 July 2022



View Online



Export Citation



CrossMark

Brianna Conrad^{a)}  and Behrang H. Hamadani 

AFFILIATIONS

National Institute of Standards and Technology, 100 Bureau Drive, Gaithersburg, Maryland 20899, USA

^{a)}Author to whom correspondence should be addressed: bsmc@alum.mit.edu

ABSTRACT

Hyperspectral electroluminescence and photoluminescence imaging of photovoltaic materials and devices produces three-dimensional spatially and spectrally resolved luminescence data, which can be calibrated to an absolute scale, enabling the extraction of high resolution maps of quantities, such as the local voltage (quasi-Fermi-level splitting). This extraction requires supplemental measurements of external quantum efficiency (EQE), but these do not have the same spatial resolution. Previously, assumptions have been made to overcome this limitation. In this work, we evaluate these assumptions for InGaAs solar cells with significant spatial variation in the luminescence spectrum shape due to small regions with elevated concentrations of radiative defects. Although appropriate for small variations in the spectral shape, we find that with more significant variation, these assumptions can result in nonphysical EQEs and too-low voltages. Combining multiple methods can help to alleviate this, or a minimum voltage map can be extracted, which will be similar to the actual voltage when EQE is high.

Published by AIP Publishing. <https://doi.org/10.1063/5.0097572>

Photoluminescence (PL) and electroluminescence (EL) have been used extensively in both imaging and spectral forms for characterization of photovoltaic materials and devices. Luminescence imaging can provide spatial information, revealing cracks, defects, grain boundaries, and other types of nonhomogeneity either inherent to the material or introduced from processing or aging.^{1–4} Luminescence spectra can provide information about the semiconductor bandgap, radiative efficiencies, absorptivity, external quantum efficiencies (EQEs), internal voltages (or quasi-Fermi level splitting), and pseudo-IV curves, among other values.^{5–9}

Hyperspectral imaging allows for the collection of spatially and spectrally resolved EL and PL data. High spectral resolution combined with radiometric calibrations of the emission signal determines luminescence flux, regardless of material or luminescence spectrum. This makes it a powerful tool able to determine those properties, such as local voltage, which are accessible by luminescence spectra for individual locations on the sample, and visualize them across the sample, identifying spatial features and nonuniformity. Alternative methods for mapping local voltage, such as Kelvin probe force microscopy and atomic force microscopy, or luminescence scanning tend to take longer, have less flexibility of spatial scale, require specific sample structures, or are highly sensitive to surface properties of the sample.^{10–13}

However, the usefulness of the spatial resolution of hyperspectral imaging can be compromised by the need for additional

measurements, which generally do not produce spatially resolved data. This has led researchers to use hyperspectral imaging data from a single location or in a spatially averaged form for the calculation of local voltages, pseudo-IV, and EQE curves.^{14–16} In other cases, assumptions are made, such as about spatial uniformity of externally measured EQE or absorptivity, for the calculation of a spatially resolved local voltage map.^{16–19}

Here, we consider the applicability of these assumptions to cases where the semiconductor band edge and the luminescence spectrum shape differ across the device area, focusing on determining the high-resolution local voltage of solar cells containing areas with high concentrations of radiative defects. The methods and considerations described will apply to any photovoltaic device with sufficient luminescence for EL/PL analysis and spatial variation in the luminescence spectrum. This includes devices with larger anomalous areas than seen in this work, and microphotovoltaic cells, where anomalous areas will have larger impact on overall device performance. In all cases, qualitative understanding of the behavior and effect of such regions is improved.

Commercial 4 cm² InGaAs on Ge solar cells with a 2% indium alloy fraction (estimated from optical modeling) was measured with a Photon ETC Grand-EOS hyperspectral imaging system, with a spectral range of 400–1600 nm and a spectral resolution of 2 nm in both EL and PL modes. EL measurements were taken with a 20 mm field of

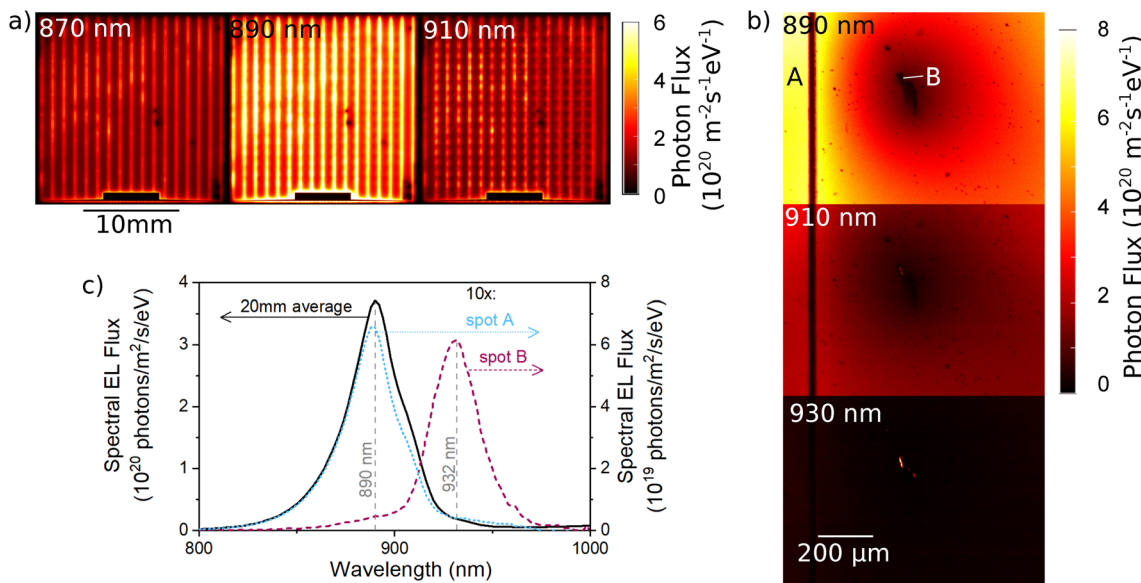


FIG. 1. (a) Absolute hyperspectral EL image cube taken with 20 mm field of view and 100 mA injected current. (b) The same, taken with 10 \times microscope objective and 25 mA injected current, centered on the region with a high concentration of radiative defects. Original image has been cropped to allow larger printing of this region. (c) Absolute EL spectra extracted from indicated spots in parts (a) and (b). Multimedia views: <https://doi.org/10.1063/5.0097572.1>; <https://doi.org/10.1063/5.0097572.2>

view, showing the full cell [Fig. 1(a), Multimedia view] and under a 10 \times microscope objective [Fig. 1(b), Multimedia view]. PL measurements were taken under a 10 \times microscope objective with 532 nm laser illumination. Absolute calibration of the image cubes is performed as described in the previous work.^{15,20} EQE measurements were taken using the differential spectral responsivity (DSR) method.²¹

Wide field EL measurements showed several dark areas, visible near the center of Fig. 1(a), which we investigated further under the 10 \times microscope objective [Fig. 1(b)]. We see that these areas are centered on small regions that show a relatively strong luminescence peak at 932 nm. This indicates a radiative defect present in large concentration in this region, with the surrounding dark area due to carriers being drained from the bulk material. We will refer to this region as the defect region. Numerous radiative defects have been identified in GaAs.^{22,23} Based on additional temperature-dependent analysis that will be treated in a future publication, the peak seen here is attributed to a Ga antisite defect.

The significant difference in the luminescence spectrum shape in the defect region presents challenges in determining the local voltage using previously employed assumptions. We first consider the smaller variations in the luminescence spectrum shape seen throughout the device and what they can tell us about appropriate methods of analysis.

The local junction voltage (V) is related to the measured electroluminescent photon flux (R) at a given energy, E , by the reciprocity relationship²⁴ as

$$R(E) = \text{EQE}(E) e^{qV/kT} B(E), \quad (1)$$

where q is the elementary charge; k is the Boltzmann constant; T is the cell temperature; EQE is the external quantum efficiency, defined as the probability that an incident photon creates a carrier, which

contributes to the light-generated current; and B is the black body spectral photon flux with

$$B(E) \cong 2\pi E^2 h^{-3} c^{-2} \exp(-E/kT), \quad (2)$$

where h is Plank's constant and c is the speed of light in a vacuum. The primary challenge in using the reciprocity relation is the interdependence of V and EQE, which introduces the need for additional external measurements.

The reciprocity relationship has also been expressed and used, primarily for determining overall cell voltage and I-V curves, as^{14,15}

$$R_{\text{tot}} = \langle \text{EQE} \rangle e^{qV/kT} \int_{E_1}^{\infty} B(E) dE, \quad (3)$$

where R_{tot} is the total photon flux out of the cell and $\langle \text{EQE} \rangle$ is a weighted average of the EQE, defined as

$$\langle \text{EQE} \rangle = \frac{\int R(E) \text{EQE}(E) dE}{\int R(E) dE}. \quad (4)$$

E_1 has previously been written as E_g and described as the semiconductor bandgap.^{14,15} However, Eqs. (1)–(4) can be rearranged to find

$$\int_{E_1}^{\infty} B(E) dE = \frac{R_{\text{tot}}^2}{\int R(E)^2 / B(E) dE}. \quad (5)$$

We do not need to calculate E_1 itself to determine the local voltage, which is advantageous as Eq. (5) must be solved numerically for E_1 . However, if we wish to map E_1 for a more intuitive interpretation of the data, a good linear fit of $\ln(\int_{E_1}^{\infty} B(E) dE)$ as a function of E_1 can be found over a moderate range (see the supplementary material).

Equation (5) shows that the spatially resolved value of E_1 can be definitively determined from just the absolute hyperspectral EL image cube. No knowledge of EQE or V is required. Figure 2 shows a map of E_1 for this cell, as well as the local EL luminescence spectrum, local relative EQE calculated with Eq. (1), and E_1 calculated with Eq. (5) for the two spots indicated (using 5×5 pixel areas). Notably, E_1 is non-uniform, potentially as a result of specific fabrication processes. It also does not correspond to the bandgap determined from the EL peak or inflection point of the local (relative) EQE curve. E_1 is, therefore, better described as an energy level, which is below most of the EL photon flux (approximately 85% in this case) and which can be calculated precisely by Eq. (5).

Although E_1 is determinable, finding V using Eq. (3) still requires knowledge of the EQE. Therefore, extracting the local voltage requires knowledge of the local EQE, which is not obtainable by the DSR method. Local relative EQE curves can be extracted by the reciprocity equation, as in Fig. 2(b), but absolute values are dependent on the local voltage. One approach is to use Eq. (1) and assume a spatially uniform EQE from the DSR measurement, which we will refer to as the “uniform EQE method” going forward. Another is to, also with Eq. (1), assume a spatially uniform EQE only for a spectral region that is both well above the bandgap and contains noticeable luminescence,^{17–19} which we will refer to as the “uniform high-energy EQE method.” For these devices, we have used an average of the EQE over the 850–870 nm range. The second option is forgiving of local variations in the EQE near the bandgap. Equation (3) also provides the option of assuming a spatially uniform $\langle \text{EQE} \rangle$, with the locally calculated E_1 , which we will refer to as the “uniform $\langle \text{EQE} \rangle (E_1)$ method.” A similar method with the locally calculated E_1 replaced by a uniform E_g based on DSR EQE measurements will be referred to as the “uniform $\langle \text{EQE} \rangle (E_g)$ method.”

We now extract and compare local voltage maps of this device using the options discussed above, with the results shown in the top row of Fig. 3, and differences between the methods shown in the bottom row. Figure 3(a) shows the voltage map extracted with the uniform high-energy EQE method, the most commonly accepted method in previous work.^{17–19} The effect of error in the EQE measurement is shown in Fig. 3(b), with a 10% error in the EQE corresponding to less than 3 mV error in voltage. Figure 3(c) shows the voltage map

extracted with the uniform EQE method, and Fig. 3(f) shows the error compared to the uniform high-energy EQE version.

Figures 3(d) and 3(e) show the voltage map calculated by the uniform $\langle \text{EQE} \rangle (E_g)$ and uniform $\langle \text{EQE} \rangle (E_1)$ methods, respectively. Figures 3(g) and 3(h) show the error using these methods compared to the uniform high-energy EQE method. The uniform $\langle \text{EQE} \rangle (E_1)$ is, as expected, consistent with the uniform high-energy EQE results, while the uniform $\langle \text{EQE} \rangle (E_g)$ results in tens of mV of nonspatially uniform error. Therefore, the qualitative understanding of the local voltage pattern is adversely affected, along with the quantitative values. The uniform EQE method results in smaller errors [Fig. 3(f)] but, due to the band edge variation present in this device (Fig. 2), also introduces spatial variation in local voltage, which is not present with the uniform high-energy EQE method. Additionally, this method can be influenced by the selection of the integration limits applied to Eq. (1), particularly the low-energy limit if the DSR-measured EQE does not go strictly to zero below the bandgap. As the DSR method is least accurate when EQE is low, errors in this range are expected.¹⁶ Based on these results, the most reliable methods for determining the local voltage in the presence of small band edge fluctuations are the uniform high-energy EQE and uniform $\langle \text{EQE} \rangle (E_1)$ methods.

We now consider more significant variations in the luminescence spectrum, in this case, regions with a high concentrations of radiative defects resulting in an EL peak at 932 nm.

Using the uniform EQE method is particularly problematic here. Doing so produces the voltage map seen in Fig. 4(a), with an apparent higher local voltage in the immediate defect region than in the surrounding area. However, this would not result in the draining of carriers from the surrounding region that is indicated by the dark area in the EL image (Fig. 1). The strong luminescence from the radiative defect might naively be expected to indicate a high voltage in this region, but this fails to take into account the rapid increase in $B(E)$ with the decrease in energy.

$B(E)$ is 12 times as high at 932 nm as it is at 890 nm, resulting in a 60 mV lower V for the same luminescence flux measured at 932 nm compared to that measured at 890 nm, assuming a constant EQE [Fig. 4(b)]. Therefore, the strong luminescence peak at 932 nm in the defect region does not necessarily indicate a higher voltage in this region. We note that this effect will also be important in applying previous

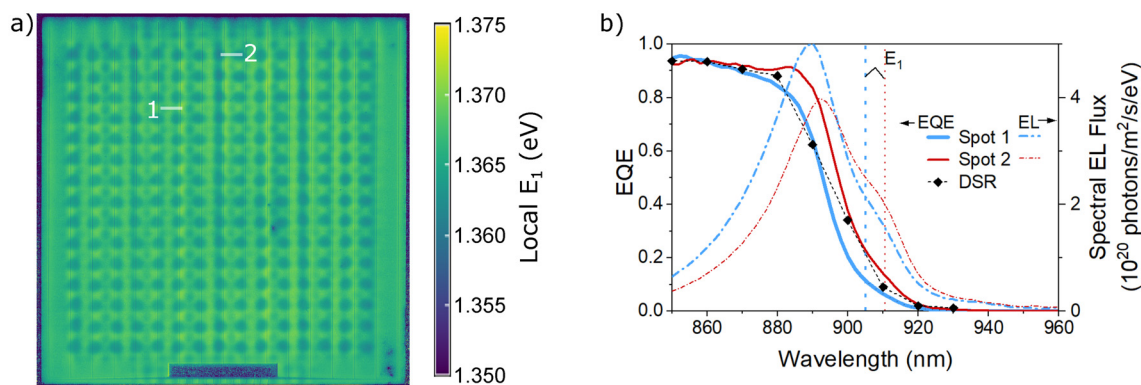


FIG. 2. (a) Map of local E_1 calculated from hyperspectral EL image cube. (b) EL spectrum, extracted local relative EQE (scaled to DSR method EQE), and E_1 for two locations indicated in (a).

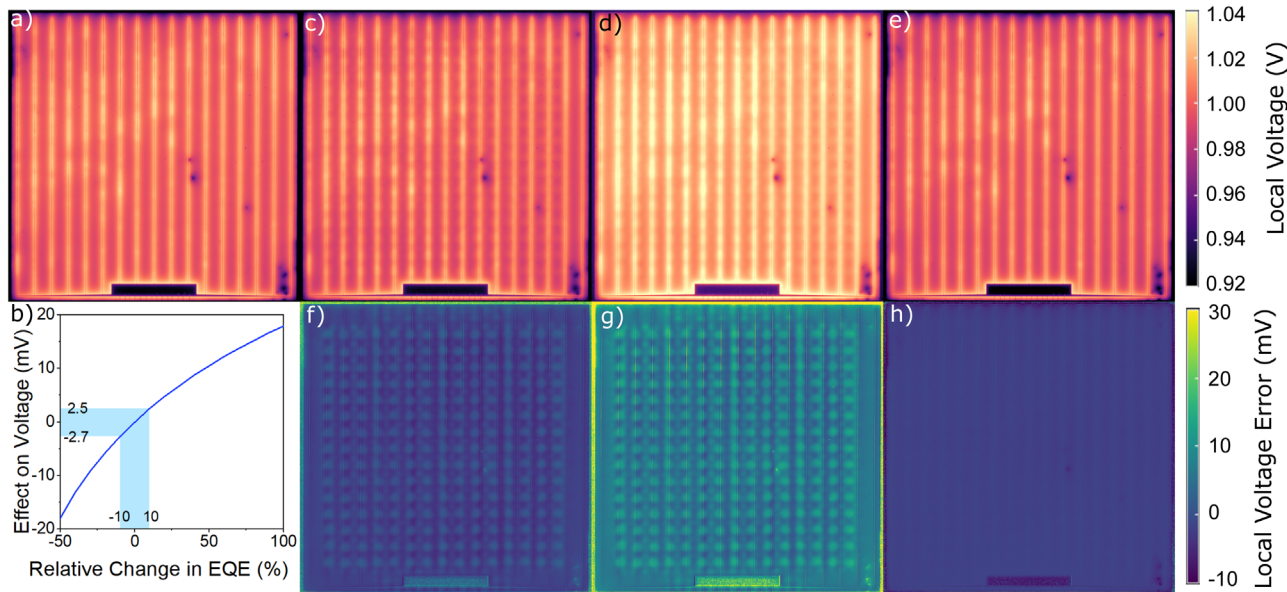


FIG. 3. Voltage maps extracted using (a) uniform high-energy EQE, (c) uniform EQE, (d) uniform $\langle \text{EQE} \rangle(E_g)$, and (e) uniform $\langle \text{EQE} \rangle(E_1)$ methods. (b) The effect that an error in EQE has on the extracted voltage, and (f)–(h) the difference between the voltage maps above and that shown in part (a).

luminescence imaging methods, such as lifetime mapping, which implicitly rely on the spatial homogeneity of the luminescence spectrum,¹ to cells with radiative defect regions or other significant spatial variation in luminescence spectrum.

We now consider the uniform high-energy EQE method. Figure 4(b) shows a relative EQE curve from a 5×5 pixel square at

the center of the defect region, scaled to match DSR-EQE between 850 and 870 nm. Not only does the shape of the EQE differ greatly from that measured by DSR or extracted from other regions of the device, this scaling results in an EQE over 100% between 912 and 934 nm. Therefore, the uniform high-energy EQE method would result in underestimation of the voltage in the defect region. The areas

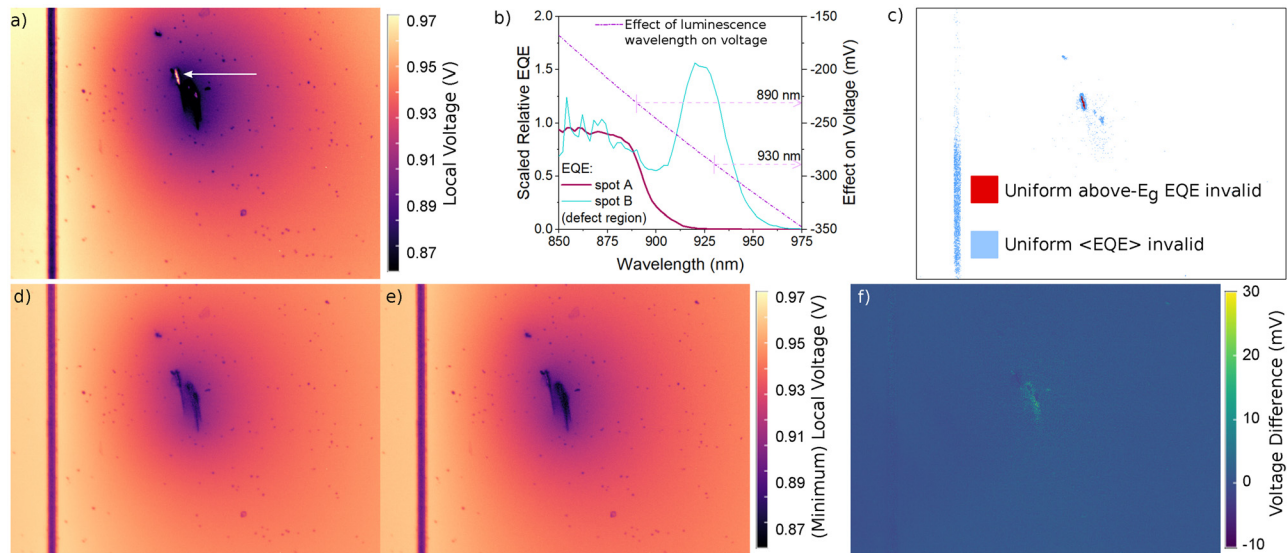


FIG. 4. (a) Local voltage map extracted from $10 \times$ EL hyperspectral image cube with the uniform EQE method. Arrow points to apparent high voltage in the defect region. (b) Local relative EQEs extracted from defect and bulk regions, scaled to DSR-EQE in high-energy region (left axis) and effect that the luminescence wavelength has on the extracted voltage (right axis, dashed line). (c) Areas for which assuming spatially uniform high-energy EQE or uniform $\langle \text{EQE} \rangle$ result in nonphysical spectral EQE. (d) Voltage map extracted using maximum of uniform high-energy EQE and uniform $\langle \text{EQE} \rangle(E_1)$ methods. (e) Minimum possible voltage map. (f) Difference between (d) and (e).

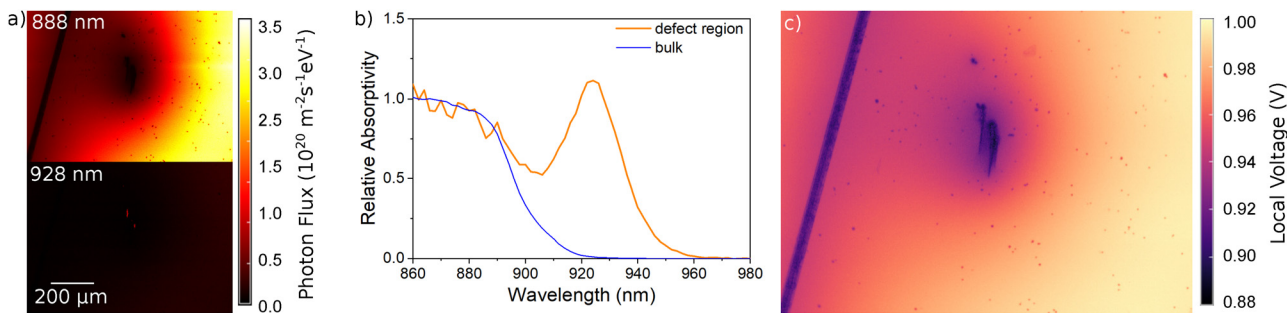


FIG. 5. (a) Two frames of a hyperspectral PL image cube, taken with a $10\times$ microscope objective and an illumination intensity of 230 mW/cm^2 . (b) Local relative A extracted from two spots. (c) Minimum voltage map extracted from the PL hyperspectral image cube.

where such an assumption results in a nonphysical EQE are shown in red in Fig. 4(c).

If we use the uniform $\langle \text{EQE} \rangle (E_1)$ method, with $\langle \text{EQE} \rangle$ calculated from the DSR-measured EQE and the spatially averaged EL spectrum, the associated EQE in the middle of the defect region remains nominally below 100%. However, around the edges of this region, where both the 890 and 932 nm peaks are present in similar intensity, the associated $\text{EQE}(E)$ becomes greater than 100%. This is due to the dependence of B on E described above. When calculating $\langle \text{EQE} \rangle$, both peaks contribute relatively equally to the denominator in Eq. (4), but the lower energy peak contributes relatively little to the numerator, as the $\text{EQE}(E)$ term is proportional to $1/B(E)$. Therefore, $\langle \text{EQE} \rangle$ in areas with two peaks of similar intensity will be lower than in areas with only one significant peak. The areas for which the maximum physical $\langle \text{EQE} \rangle$ is less than 95% of our uniform value are shown in blue in Fig. 4(c) and have little overlap with the regions for which the uniform high-energy EQE is nonphysical. As using a higher EQE results in extracting a lower voltage [Eq. (1)], we eliminate the nonphysical (too-high EQE) region by taking the maximum voltage from the uniform high-energy EQE and uniform $\langle \text{EQE} \rangle$ methods, to find the voltage map shown in Fig. 4(d). Using each method alone results in voltages up to 22 meV lower in or near the defect region of this sample.

Having noted that we are limited by the physical requirement that EQE not be above 100%, we can also calculate a local minimum voltage map, which is the voltage map if we use Eq. 1 and determine the EQE of each pixel by scaling the relative EQE such that its spectral maximum is 100%. We do this using the average value between 850 and 870 nm (to reduce noise where luminescence is low) and the maximum value between 920 and 940 nm and find the map as shown in Fig. 4(e). Figure 4(f) shows the difference between the method described in the previous paragraph and the minimum voltage. In the bulk of the device, where the higher energy peak dominates, the two are very similar due to the high EQE of the device. Either of these methods, therefore, provides a reasonable map of the local voltage in such a situation. If the device EQE is known to be significantly lower than 100%, the first method may be more appropriate, or the minimum voltage can be calculated by scaling for a different maximum $\text{EQE}(E)$ in each pixel.

The aforementioned methods are also applicable to PL measurements, using the generalized Planck equation, which follows the form of Eq. (1), with EQE replaced by the absorptivity A (the probability that a photon incident on the surface will be absorbed). It has been

previously stated that, for solar cells, A can be taken to be 1 at energies above the bandgap and 0 at energies below the bandgap.^{17,25} PL hyperspectral imaging of this device [Fig. 5(a)], however, shows that inside the defect region, A is higher around 930 nm than in the above-bandgap range [Fig. 5(b)]. Therefore, we scale A such that the spectral maximum is equal to 1, producing a minimum voltage map as in Fig. 5(c) as a good approximation for the local voltage in this case. At this illumination condition, the voltage in the defect area is about 100 mV lower than in bulk locations a similar distance from the metal finger, compared to the 60 meV difference in luminescence peak energies and local E_1 . This could indicate that the high concentration of defects in this region also increases nonradiative recombination.

The determination of high-resolution spatially resolved local voltage in photovoltaic devices and materials from absolutely calibrated hyperspectral EL and PL image cubes can be a valuable characterization tool but requires the application of certain assumptions as to device EQE or absorptivity. If local variations are small, an assumption of a uniform high-energy EQE or A may be valid, but when hyperspectral imaging reveals small regions with a high concentration of radiative defects, or other significant variations in spectral luminescence shape, this assumption cannot be used uncritically. Attention must be paid, in particular, to ensure that scaling EQE or A by one spectral region does not result in nonphysical values of EQE or A in another spectral region. The correct use of an alternate form of the reciprocity or generalized Planck equation can extend the spatial region for which a valid scaling can be achieved. In extreme cases, only a local minimum voltage map may be extractable, but even this can provide valuable information.

See the [supplementary material](#) for a detailed explanation and demonstration of the fitting of fitting to determine E_1 .

Certain commercial equipment, instruments, software, or materials are identified in this paper to specify the experimental procedure adequately. Such identification is not intended to imply recommendation or endorsement by the National Institute of Standards and Technology nor is it intended to imply that the materials or equipment identified is necessarily the best available for the purpose.

AUTHOR DECLARATIONS

Conflict of Interest

The authors have no conflicts to disclose.

Author Contributions

Brianna Conrad: Conceptualization (equal); Investigation (lead); Methodology (lead); Visualization (lead); Writing – original draft (lead); Writing – review and editing (equal). **Behrang H. Hamadani:** Conceptualization (equal); Methodology (supporting); Resources (lead); Supervision (lead); Writing – review and editing (equal).

DATA AVAILABILITY

The data that support the findings of this study are available from the corresponding author upon reasonable request.

REFERENCES

- ¹T. Trupke, R. Bardos, M. Abbott, E. Pink, Y. Augarten, F. Chen, K. Fisher, J. Cotter, M. Kasemann, M. Rüdiger, S. Kontermann, M. Schubert, M. The, S. Glunz, W. Warta, P. Wuerfel, D. Macdonald, J. Tan, A. Cuevas, and J. Fernandez, "Progress with luminescence imaging for the characterisation of silicon wafers and solar cells," in *Proceedings of the 22nd European Photovoltaic Solar Energy Conference* (IEEE, 2007), pp. 22–31.
- ²J. Haunschmid, M. Glatthaar, M. Demant, J. Nievendick, M. Motzko, S. Rein, and E. R. Weber, "Quality control of as-cut multicrystalline silicon wafers using photoluminescence imaging for solar cell production," *Sol. Energy Mater. Sol. Cells* **94**, 2007–2012 (2010).
- ³B. Du, R. Yang, Y. He, F. Wang, and S. Huang, "Nondestructive inspection, testing and evaluation for Si-based, thin film and multi-junction solar cells: An overview," *Renewable Sustainable Energy Rev.* **78**, 1117–1151 (2017).
- ⁴R. Bhoothpathy, O. Kunz, M. Juhl, T. Trupke, and Z. Hameiri, "Outdoor photoluminescence imaging of photovoltaic modules with sunlight excitation," *Prog. Photovoltaics* **26**, 69–73 (2018).
- ⁵G. D. Pettit, J. M. Woodall, and H. J. Hovel, "Photoluminescent characterization of GaAs solar cells," *Appl. Phys. Lett.* **35**, 335–337 (1979).
- ⁶T. Trupke, E. Daub, and P. Würfel, "Absorptivity of silicon solar cells obtained from luminescence," *Sol. Energy Mater. Sol. Cells* **53**, 103–114 (1998).
- ⁷V. Rumyantsev and J. Rodriguez, "Luminescent characterization of contactless AlGaAs/GaAs heterostructure for solar cells and diodes," *Sol. Energy Mater. Sol. Cells* **31**, 357–370 (1993).
- ⁸T. Kirchartz, U. Rau, M. Kurth, J. Mattheis, and J. Werner, "Comparative study of electroluminescence from Cu(In,Ga)Se₂ and Si solar cells," in *Proceedings of Symposium O on Thin Film Chalcogenide Photovoltaic Materials, EMRS 2006 Conference [Thin Solid Films]* **515**, 6238–6242 (2007).
- ⁹T. Kirchartz, U. Rau, M. Hermle, A. W. Bett, A. Helbig, and J. H. Werner, "Internal voltages in GaInP/GaInAs/Ge multijunction solar cells determined by electroluminescence measurements," *Appl. Phys. Lett.* **92**, 123502 (2008).
- ¹⁰K. Dirscherl, I. Baikie, G. Forsyth, and A. van der Heide, "Utilisation of a micro-tip scanning Kelvin probe for non-invasive surface potential mapping of mc-Si solar cells," *Sol. Energy Mater. Sol. Cells* **79**, 485–494 (2003).
- ¹¹T. Trupke, R. A. Bardos, M. C. Schubert, and W. Warta, "Photoluminescence imaging of silicon wafers," *Appl. Phys. Lett.* **89**, 044107 (2006).
- ¹²E. M. Tennyson, J. L. Garrett, C. Gong, J. A. Frantz, J. D. Myers, R. Y. Bekele, J. S. Sanghera, J. N. Munday, and M. S. Leite, "Assessing local voltage in cigs solar cells by nanoscale resolved kelvin probe force microscopy and sub-micron photoluminescence," in *2014 IEEE 40th Photovoltaic Specialist Conference (PVSC)* (IEEE, 2014), pp. 0691–0694.
- ¹³A. Longacre, M. Martin, T. Moran, O. V. Kolosov, E. Schneller, A. J. Curran, M. Wang, J. Dai, L. S. Bruckman, J. Jaubert, K. O. Davis, J. L. Braid, R. H. French, and B. D. Huey, "Direct nanoscale mapping of open circuit voltages at local back surface fields for PERC solar cells," *J. Mater. Sci.* **55**, 11501–11511 (2020).
- ¹⁴S. Chen, L. Zhu, M. Yoshita, T. Mochizuki, C. Kim, H. Akiyama, M. Imaizumi, and Y. Kanemitsu, "Thorough subcells diagnosis in a multi-junction solar cell via absolute electroluminescence-efficiency measurements," *Sci. Rep.* **5**, 7836 (2015).
- ¹⁵B. H. Hamadani, "Understanding photovoltaic energy losses under indoor lighting conditions," *Appl. Phys. Lett.* **117**, 043904 (2020).
- ¹⁶A. Delamarre, L. Lombez, and J.-F. Guillemoles, "Characterization of solar cells using electroluminescence and photoluminescence hyperspectral images," *J. Photonics Energy* **2**, 027004–027009 (2012).
- ¹⁷A. Delamarre, D. Ory, M. Paire, D. Lincot, J.-F. Guillemoles, and L. Lombez, "Evaluation of micrometer scale lateral fluctuations of transport properties in CIGS solar cells," in *Physics, Simulation, and Photonic Engineering of Photovoltaic Devices II*, edited by A. Freundlich and J.-F. Guillemoles (SPIE International Society for Optics and Photonics, 2013), Vol. 8620, pp. 53–59.
- ¹⁸G. El-Hajje, C. Momblona, L. Gil-Escríg, J. Avila, T. Guillermot, J.-F. Guillemoles, M. Sessolo, H. J. Bolink, and L. Lombez, "Quantification of spatial inhomogeneity in perovskite solar cells by hyperspectral luminescence imaging," *Energy Environ. Sci.* **9**, 2286–2294 (2016).
- ¹⁹R. Tamaki, Y. Shoji, L. Lombez, J.-F. Guillemoles, and Y. Okada, "Quantitative analysis of InAs quantum dot solar cells by photoluminescence spectroscopy," in *Physics, Simulation, and Photonic Engineering of Photovoltaic Devices VII*, edited by A. Freundlich, L. Lombez, and M. Sugiyama (SPIE International Society for Optics and Photonics, 2018), Vol. 10527, pp. 141–147.
- ²⁰S. M. Chavali, J. Roller, M. Dagenais, and B. H. Hamadani, "A comparative study of subcell optoelectronic properties and energy losses in multijunction solar cells," *Sol. Energy Mater. Sol. Cells* **236**, 111543 (2022).
- ²¹B. H. Hamadani, J. Roller, B. Dougherty, F. Persaud, and H. W. Yoon, "Absolute spectral responsivity measurements of solar cells by a hybrid optical technique," *Appl. Opt.* **52**, 5184–5193 (2013).
- ²²V. Swaminathan, "Defects in GaAs," *Bull. Mater. Sci.* **4**, 403–442 (1982).
- ²³N. H. Ky and F. K. Reinhart, "Amphoteric native defect reactions in Si-doped GaAs," *J. Appl. Phys.* **83**, 718–724 (1998).
- ²⁴U. Rau, "Reciprocity relation between photovoltaic quantum efficiency and electroluminescent emission of solar cells," *Phys. Rev. B* **76**, 85303 (2007).
- ²⁵L. Hirst, *Principles of Solar Energy Conversion* (Elsevier, London, 2012), pp. 305–307.

Local Voltage Mapping of Solar Cells in the Presence of Localized Radiative Defects: Supplemental Material

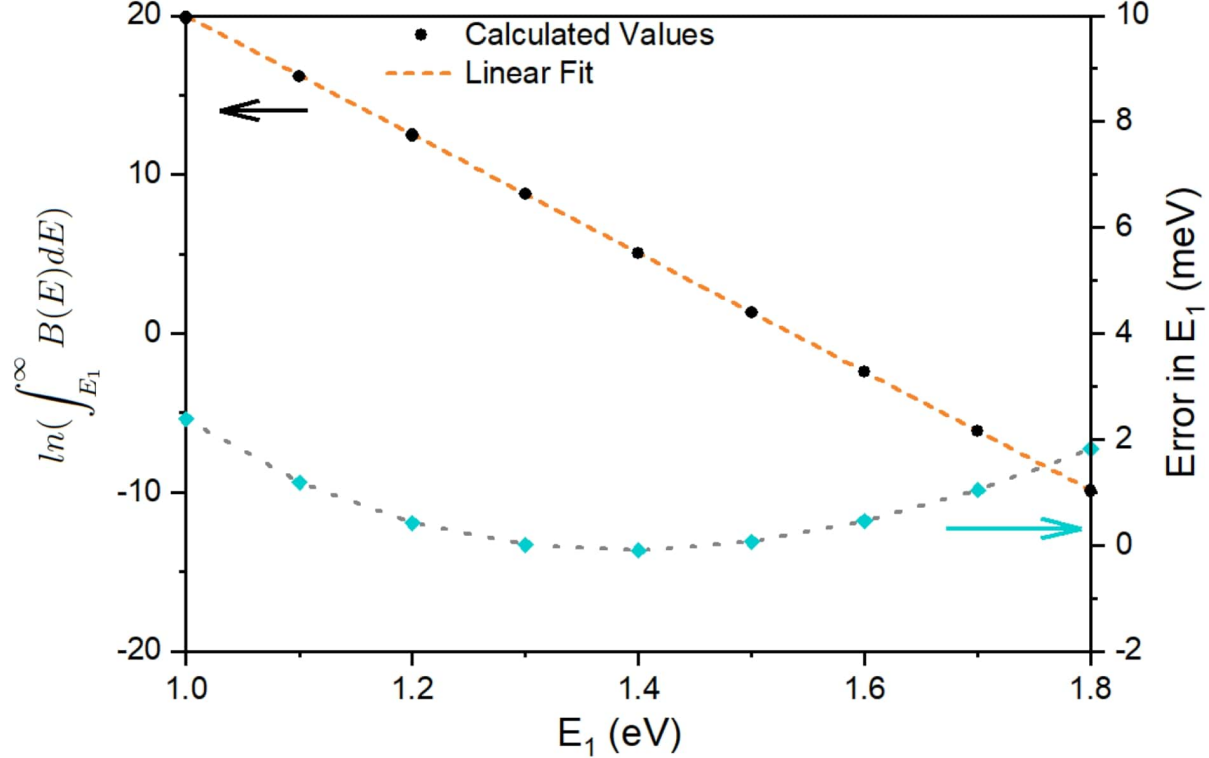


FIG. S1. Plot of logarithm of integral seen in Eqn. 5 as a function of E_1 , with linear fit over a moderate energy range. The error in E_1 between the linear fit and the numerically calculated values are plotted on the right y-axis.

DETERMINING E_1 USING LINEAR FIT

After calculating $\ln(\int_{E_1}^{\infty} B(E)dE)$ as a function of E_1 for several values of E_1 (black circles in Fig. S1), using $B(E)$ as defined in Eqn. 2 in the main text, a linear fit is found such that

$$\ln\left(\int_{E_1}^{\infty} B(E)dE\right) = mE_1 + b \quad (\text{S1})$$

with m (slope) and b (intercept) being fitting parameters. Eqn. S1 can be rearranged so that E_1 can be calculated as:

$$E_1 = \frac{1}{m} \left[\ln \left(\int_{E_1}^{\infty} B(E) dE \right) - b \right] \quad (\text{S2})$$

The difference between the original E_1 and that determined from Eqn. S2 is also plotted in Fig. S1.